Chemical Science

EDGE ARTICLE

M. Eugenia Pérez-Ojeda, Andreas Hirsch *et al.*
Diastereoselective formation of homochiral flexible perylene
bisimide cyclophanes and their hybrids with fullerenes

EDGE ARTICLE

Diastereoselective formation of homochiral flexible perylene bisimide cyclophanes and their hybrids with fullerenes†‡

Iris Solymosi, [iD] §[a] Swathi Krishna,§[b] Edurne Nuin, [iD] [c] Harald Maid,[a] Barbara Scholz, [iD] [a] Dirk M. Guldi, [iD] [b] M. Eugenia Pérez-Ojeda [iD] *[a] and Andreas Hirsch [iD] *[a]

Cyclophanes of different ring sizes featuring perylene-3,4:9,10-tetracarboxylic acid bisimide (PBI) linked by flexible malonates were designed, synthesized, and investigated with respect to their structural, chemical and photo-physical properties. It is predominantly the number of PBIs and their geometric arrangement, which influence dramatically their properties. For example, two-PBI containing cyclophanes reveal physico-chemical characteristics that are governed by strong co-facial π–π interactions. This is in stark contrast to cyclophanes with either three or four PBIs. Key to co-facial π–π stackings are the flexible malonate linkers, which, in turn, set up the ways and means for diastereoselectivity of the homochiral PBIs at low temperatures, on one hand. In terms of selectivity, diastereomeric $(M,M)/(P,P) : (M,P)/(P,M)$ pairs with a ratio of approximately 10 : 1 are discernible in the ^{1}H NMR spectra in $C_2D_2Cl_4$ and a complete diastereomeric excess is found in CD_2Cl_2. On the other hand, symmetry-breaking charge transfer as well as charge separation at room temperature are corroborated in steady-state and time-resolved photo-physical investigations. Less favourable are co-facial π–π stackings in the three-PBI containing cyclophanes. For statistical reasons, the diastereoisomers $(M,M,M)/(P,P,P)$ and $(M,M,P)/(P,P,M)$ occur here in a ratio of 1 : 3. In this case, symmetry-breaking charge transfer as well as charge separation are both slowed down. The work was rounded-off by integrating next to the PBIs, for the first time, hydrophobic or hydrophilic fullerenes into the resulting cyclophanes. Our novel fullerene–PBI cyclophanes reveal unprecedented diastereoselective formation of homochiral $(M,M)/(P,P)$ pairs exceeding the traditional host–guest approach. Hybridization with fullerenes allows us to modulate the resulting solubility, stacking, cavity and chirality, which is of tremendous interest in the field.

Introduction

Following the discovery of [2.2]paracyclophane by Brown and Farthing[1] and its targeted synthesis with high dilution by Cram and Steinberg,[2] cyclophanes have gained more and more importance in recent decades. For our macrocycles, PBIs were chosen as building blocks owing to their unique physico-

[a]Department of Chemistry and Pharmacy, Friedrich-Alexander-University Erlangen-Nuremberg, Nikolaus-Fiebiger-Straße 10, 91058 Erlangen, Germany. E-mail: andreas.hirsch@fau.de; eugenia.perez-ojeda@fau.de
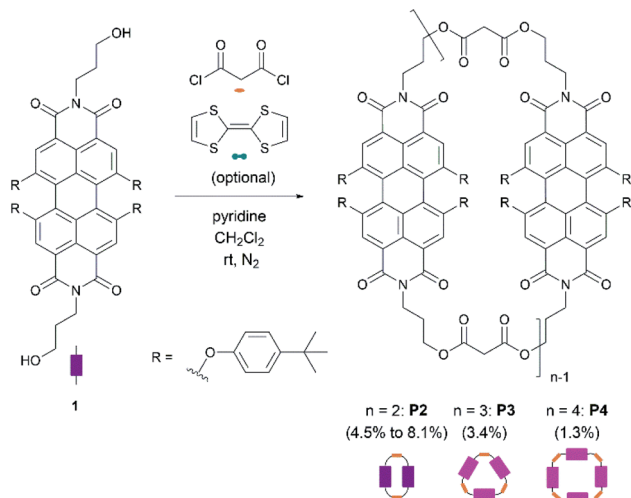
[b]Department of Chemistry and Pharmacy, Friedrich-Alexander-University Erlangen-Nuremberg, Egerlandstraße 3, 91058 Erlangen, Germany. E-mail: dirk.guldi@fau.de

[c]Instituto de Ciencia Molecular (ICMol), Universidad de Valencia, Catedrático José Beltrán 2, Paterna 46980, Spain

† In memory of Prof. Dr Klaus Hafner.

‡ Electronic supplementary information (ESI) available: Experimental details including HPLC, NMR, mass, UV-vis, fluorescence, spectroelectrochemistry, transient absorption spectra and fluorescence emission–excitation matrix. See DOI: 10.1039/d1sc04242d

§ These authors contributed equally.

chemical as well as thermal properties and, in turn, great potential for applications.[3] PBIs are, for example, used as semiconductors in field effect transistors (FETs)[4–6] or as components in various solar cells.[7,8] In addition, they self-organize based on π–π interactions.[9,10] PBI containing cyclophanes have recently received increasing attention. Leading examples from Würthner's group are the demonstration of tunable electronic interactions between PBIs[11] or of fluorescent sensing to detect electron-rich and electron-poor guests.[12] Within the cyclophanes, the PBIs are held together *via* either flexible[13–15] or rigid linkers.[12,16] Notably, the linker conditions the cavity given by the cyclophanes. This has resulted in incorporating small aromatic hydrocarbons,[12,17] homochiral molecules,[17,18] and fullerenes.[19] Despite the fact that flexible and long linkers make the incorporation rather difficult due to PBI self-aggregation, fullerenes have even been encapsulated in a PBI-containing macrocycle with flexible linkers.[19] Strong π–π interactions are, however, advantageous for promoting the cyclization through self-organization[14,20] Traditionally, cyclization has been favored over oligomerization by either high dilutions[13,19,21] or templating effects.[12,22] Up to six[23] or

Scheme 1 Cyclization reaction for the synthesis of PBI-based macrocycles **P2**, **P3**, and **P4**.

even nine PBIs[24] within a macrocycle have been incorporated and isolated so far.

Controlling the size of the cyclophanes and the arrangement of the molecular building blocks therein ultimately governs the properties and, in turn, determines the incorporation of molecular guests. Thus, in the current contribution we have also tackled the template effect to favor a dimeric PBI-arrangement and compared the π–π stacking interactions in two-PBI-containing cyclophanes with those featuring either three or four PBIs. Importantly, PBIs were linked through flexible malonate linkers to enable the functionalization of the

Fig. 1 MALDI-TOF spectrum of a fraction already purified by size exclusion and column chromatography in order to identify the bigger cycles (pos. mode, DCTB in CH$_2$Cl$_2$).

cyclic dimer with hydrophobic and hydrophilic fullerenes.[25] Incentives to control the cyclophane surroundings were to tune the physico-chemical characteristics and to alter bindings of guests through, for example, hydrophobic effects and other non-covalent interactions. To the best of our knowledge, no PBI-based cyclophanes have ever been functionalized with fullerenes with the objective to investigate such a sophisticated molecular design.

Results and discussion

Synthesis

Scheme 1 shows the synthetic procedure of cyclophanes starting from N,N'-dihydroxypropyl-1,6,7,12-tetrakis-(4-*tert*-butylphenoxy)-3,4:9,10-perylenetetracarboxydiimide **1**, which was prepared in a two-step synthesis according to modified literature procedures.[26,27] Cyclization of **1**[28,29] with malonyl dichloride using pyridine[30] as a base provides **P2**, **P3**, and **P4** as purple solids in 8.1%, 3.4%, and 1.3% yields, respectively. **2–4** indicate the associated number of PBIs (**P**) in the ring.

A generalized methodology, which promotes intramolecular ring closure based on the Ziegler–Ruggli principle, takes place under high dilution conditions to avoid polymerization reactions.[31] For this purpose, malonyl dichloride was slowly added using an automatic syringe pump over time during the reaction. In addition to **P2**, larger macrocycles as well as open-chain oligomers and polymers were formed. They were detected in MALDI-TOF experiments (Fig. 1). Due to the difficult isolation and scarce yields, macrocycles larger than **P4** were not further investigated.

To promote the formation of a specific macrocycle size, numerous intramolecular ring closure conditions were tested. To this end, several addition time spans, dilutions, and stoichiometries were investigated – Table 1. First, the addition time of one equivalent of malonyl dichloride was investigated in CH$_2$Cl$_2$ in a range from 1 to 30 h.

Based on MALDI-TOF and HPLC experiments, which revealed only traces of **P2** even after prolonged malonyl additions, the addition time span was set to 3 h per equivalent (experiments A–E). Second, the dilution conditions were examined. Reaction of **1** with malonyl dichloride at very low concentrations affords **P2** in a 2.7% yield (Table 1, experiment A). Higher concentrations of both building blocks resulted in an increased two-PBI cyclophane yield (Table 1, experiments B and
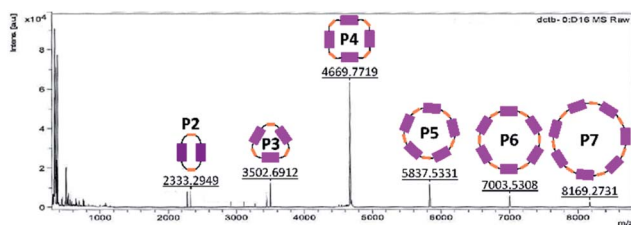
Table 1 Reaction conditions for the different cyclization experiments

EN[a]	Ratio[b] ■:–:••	c(■)[c] [mmol L^{-1}]	c(–)[d] [μmol L^{-1}]	t_{add}[e] [h]	t_{stir}[f] [d]	(○■)[%]
A	1 : 1 : 0	197	2.44	3	6	2.7
B	1 : 1 : 0	515	20.4	3	8	4.5
C	1 : 1 : 0	515	20.4	3	6	4.2
D	1 : 1 : 0.5	515	20.4	3	7	7.2
E	1 : 4 : 0.5	515	4 × 24.4	4 × 3	3	8.1
F	1 : 3 : 0	515	48.8	3	1	8.1

[a] Number of experiment. [b] Ratio of precursor **1** : malonyl dichloride : TTF. [c] Concentration of precursor molecule **1** in the reaction mixture. [d] Concentration of malonyl dichloride in the syringe. [e] Addition time span of malonyl dichloride. [f] Time of stirring (r.t.).

C) revealing that dilution optimization of the reaction conditions is crucial in the overall formation of **P2**. Furthermore, the reproducibility of all of these conditions was proven in experiment C. The macrocycle fraction was purified by size exclusion chromatography (Biobeads S-X1, dry mesh size: 28–74 μm, CH_2Cl_2) followed by column chromatography (SiO_2, using different solvent gradients depending on the macrocycle). Moreover, the separation and characterization of **P3** (3.4%) and **P4** (1.3%) were successful as well.

Prearranging the building blocks through a template effect[32,33] is expected to favor their spatial disposition to afford specific cyclophane geometries and sizes. Specifically, considering the electron-acceptor strength of PBIs, we argued that an electron-donating tetrathiafulvalene[34] (TTF) should serve as a template.[35] TTF is oxidized in cyclic voltammetry experiments at +0.34 and +0.71 V *vs.* Ag/AgCl in CH_2Cl_2,[36] while PBI is reduced at −1.08 and −1.23 V *vs.* Fc/Fc$^+$ in CH_2Cl_2.[37] According to these reduction and oxidation potentials, electron donor–acceptor interactions are likely to promote a pre-arranged, sandwich-like structure, which favors the formation of the two-PBI ring, similar to the template-controlled synthesis of tetracationic macrocycles by Stoddart.[38] As such, the cyclization reaction was carried out in the presence of TTF (experiment D) to give **P2** in 7.2% yield. This is a 1.6-fold enhancement relative to experiment B. TTF was easily removed from **P2** by size-exclusion chromatography using CH_2Cl_2 as the eluent due to its relatively weak supramolecular interaction.

Non-reacted starting material **1** was recovered under the reaction conditions in experiments A to D as detected by HPLC (*vide infra*). Thus, in another approach malonyl dichloride was added to the reaction mixture until all of **1** was consumed with or without any templating agent. Here, when TTF is present in the reaction mixture (experiment E), the yield of **P2** was raised to 8.1%, which is slightly larger than the 7.2% yield seen in the templated experiment D. An excess of malonyl dichloride improves the yields of **P2**, but at the expense of higher polymer formation. The latter were successfully separated from the crude mixture by size-exclusion chromatography as part of a more straightforward purification process. When the cyclization reaction was carried out with an excess of malonyl dichloride and without any TTF (experiment F), **P2** was furnished in 8.1% as in experiment E. This fact reveals that either the TTF-templated synthesis or the use of an excess of malonyl dichloride results in increased **P2** formation. However, the combination of both strategies in the same cyclization reaction does not result in a cooperative yield increase. To better exploit the template effect, other planar electron-rich aromatic hydrocarbons such as anthracene are foreseeable as template molecules given that the binding interaction with PBI cyclophanes has already been demonstrated.[12]

Reaction control by analytical HPLC

The reaction course as well as the product distribution under each reaction conditions were monitored with analytical high-performance liquid chromatography (HPLC) with a Nucleosil column (EC250/4 Nucleosil 100–5) using CH_2Cl_2 : ethyl

acetate : MeOH 1 : 0 : 0 → 75 : 20 : 5 as the mobile phase. HPLC profiles of experiment A (high dilution), experiment C (low dilution) and isolated **P2**, **P3**, and **P4** are shown in Fig. S1 (in the ESI‡). Despite the fact that **P2**, **P3**, and **P4** were detected in the crude mixture, as well as other by-products, their UV-vis spectra could not be compared quantitatively, due to their different spectral intensities as well as their different ε values (the detailed photophysical information is shown below).

When HPLC measurements of experiments A, C, and D were performed, a relatively large amount of unreacted starting material **1** was detected at an elution time of 17 min. Another peak with an elution time of 20 min was assigned to **P2$_{open}$** in agreement with MALDI-TOF measurements. Mass spectra as well as the corresponding molecular structure of **P2$_{open}$**, are presented in Fig. S1 (in the ESI‡). **P2$_{open}$** paves the way for the synthesis of more complex asymmetric hetero-structures when combined with other building blocks.

In addition, HPLC studies of the crude mixture using the TTF-template (experiment D) were carried out. Under these conditions, **P2** and TTF were detected separately (Fig. S3 in the ESI‡). This confirms that the interactions between **P2** and TTF are weak, which is in agreement with our previous observations during the purification size-exclusion by chromatography. TTF ensures the necessary pre-arrangement of **1** to undergo cyclization, but also enables the target to be separated from the template. Finally, when an excess of malonyl dichloride was used in the cyclization reaction (experiment E, Fig. S4 in the ESI‡), an increased **P2** peak intensity in the HPLC profiles went hand-in-hand with decreased peak intensities for **1** and **P2$_{open}$**.
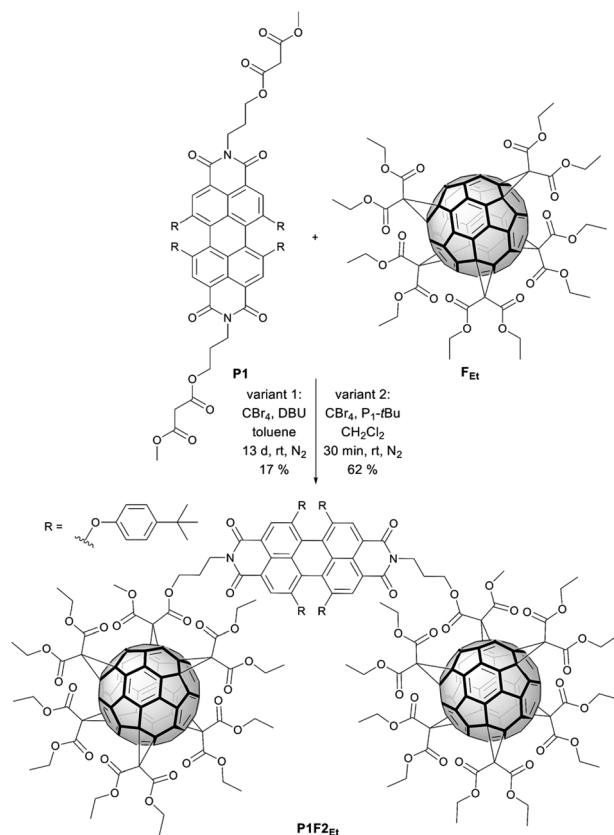
Functionalisation with fullerene pentakisadducts

The incentive to incorporate fullerenes was to exploit them as bulky molecular scaffolds, which assist in modifying the chemical environment of the cyclophane. For this purpose, flexible malonates were chosen as linkers between the PBIs to open the pathway towards the macrocycle functionalization with fullerenes. Thus, **P2** was derivatized with fullerene pentakisadducts bearing different malonate ester groups. Chemical modification of the environment *via* functionalized fullerenes with hydrophobic or hydrophilic substituents will, in turn, tune the molecular properties and facilitate the study of inter-PBI interactions. We envisioned that the modulation of π–π stacking forces will drive the dynamics of intramolecular PBI self-assembly and chiral interaction. Preparation of **P2F2$_{Et}$** and **P2F2$_{TEG}$** (Scheme 3) as well as reference **P1F2$_{Et}$** (Scheme 2) was carried out by means of the Bingel–Hirsch cyclopropanation of the corresponding malonates with ethyl (Et) or tetraethylene glycol (TEG) substituted fullerene pentakisadducts. These were prepared in a two-step synthesis as described by Pérez-Ojeda *et al.*[25] Under these conditions, **P2F2$_{Et}$**, **P2F2$_{TEG}$**, and **P1F2$_{Et}$** were obtained in 70%, 27%, and 62% yields, respectively.

Synthesis of a model compound

Reference **P1F2$_{Et}$** with only one PBI (**P1**, in the ESI‡) as a bridge between two fullerenes with ethyl substituents (**F2$_{Et}$**) was synthesized (Scheme 2). This is similar to two fullerenes bridged
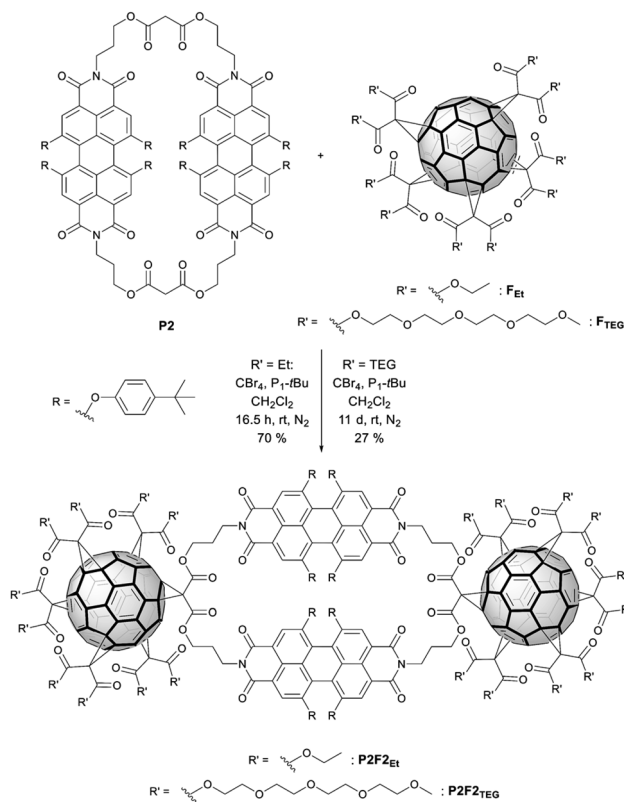
Scheme 2 Two different variants for the synthesis of reference **P1F2**$_{Et}$.

Scheme 3 Synthesis of the functional hybrids **P2F2**$_{Et}$ and **P2F2**$_{TEG}$.

to one another *via* a naphthalene bisimide-containing bis(ethyl malonate) as described by Nishimura *et al.*[39],¶ Typical Bingel–Hirsch conditions were used for the preparation of the reference compound. **P1F2**$_{Et}$ was obtained in one-step from **P1** by a reaction with fullerene pentakisadduct **F**$_{Et}$ using CBr$_4$ and 1,8-diazabicycloundec-7-ene (DBU) in toluene (Scheme 2, variant 1).[40] **P1F2**$_{Et}$ was isolated as a purple solid in 17% yield. To overcome the low yield of **P1F2**$_{Et}$, we modified in a second approach our reaction conditions, which are shown in Scheme 2 (variant 2). DBU was replaced by the Schwesinger phosphazene base P$_1$-*t*Bu for the *in situ* generation of α-bromo-malonate. CH$_2$Cl$_2$ was used as a solvent rather than toluene.[41–43] Under these conditions, **P1** was completely converted after a few minutes and **P1F2**$_{Et}$ was afforded in 62% yield.

Synthesis of functional hybrids

With the optimized conditions at hand, **P2F2**$_{Et}$ and **P2F2**$_{TEG}$ were prepared in 70% and 27% yields, respectively (Scheme 3). It is worth noting that for a complete derivatization of **P2** more equivalents of CBr$_4$ and P$_1$-*t*Bu had to be used than in the **P1F2**$_{Et}$ preparation. Owing to the large steric hindrance of the TEG chains, the reaction time for forming **P2F2**$_{TEG}$ was significantly longer and only a moderate yield of 27% was isolated in comparison with **P2F2**$_{Et}$. Interestingly, in the synthesis of the cyclophanes endowed with two fullerenes, a by-product **P2F1**$_{TEG}$ with only one fullerene and two bromine substituents was isolated. Its structure was confirmed by the isotopic pattern of

a high-resolution mass spectrum (Fig. S37 in the ESI‡) and by ^{1}H-NMR integration. Our methodology allows PBI-cyclophane functionalization not only with fullerene derivatives bearing different substituents to tune their solubility, but also with pristine fullerenes to use the resulting hybrid for optoelectronic applications of high interest and demand.[44] Thus, this simple and innovative molecular design represents a groundbreaking strategy towards a new generation of optical materials with tailored properties.
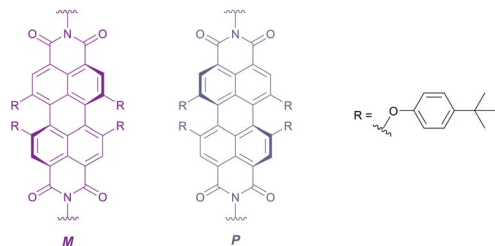
The reference as well as the functional hybrids were investigated using spectroscopic methods. The corresponding structures were unambiguously characterized by HRMS, NMR (^{1}H and ^{13}C) as well as UV-vis and fluorescence spectroscopies.

Due to the different amount of PBIs and their arrangements within the cyclophanes, intramolecular π–π stacking interactions prevail in **P2**. This leads to a spectrum, which differs from **P3** and **P4**. In addition, the presence of fullerenes has a profound influence on the properties in comparison to **P2**. To examine the structure–property relationship, temperature-dependent NMR, steady-state UV-vis, and fluorescence spectroscopy and transient absorption experiments were carried out.

Temperature-dependent ^{1}H NMR spectroscopy

Concerning NMR spectroscopy, symmetry changes due to dynamic processes and their timescales play an important role and have to be considered. Bay-substituted perylenes are

Scheme 4 Representation of the stereochemistry of the PBI atropisomers M (purple) and P (grey).

twisted rather than planar due to the steric hindrance of their substituents.[45] Therefore, two atropisomers (M/P) of lower symmetry, compared to flat perylene, exist (Scheme 4). For substituents like 4-*tert*-butylphenoxy it is, however, known that the $M \leftrightarrow P$ interconversion (butterfly dynamic) is fast at room temperature.[46] For this reason, NMR spectra are expected, which reflect higher symmetry, including symmetry elements of the second kind such as mirror planes. In particular, we awaited ^{1}H-NMR spectra compatible with point groups of D_{2h} for **P1**, **P2**, **P1F2$_{Et}$**, and **P2F2$_{Et}$**, D_{3h} for **P3** as well as D_{4h} for **P4**.

The ^{1}H-NMR spectra of **P1–P4** in CDCl$_3$ measured at room temperature are presented in Fig. 2. Reference **P1** shows a single set of sharp signals indicating fast atropisomerization of the M and P isomers. Between 8.5 and 6.5 ppm, we see a singlet for the PBI-protons (Fig. 2, a) and two multiplets for the AA′BB′ spin system of the *para*-substituted system of the aromatic bay-substituents (Fig. 2, b and c). The three CH$_2$-groups of the alkyl chain appear as two signals, a triplet like multiplet at 4.2 ppm for the almost isochronous protons of the methylene
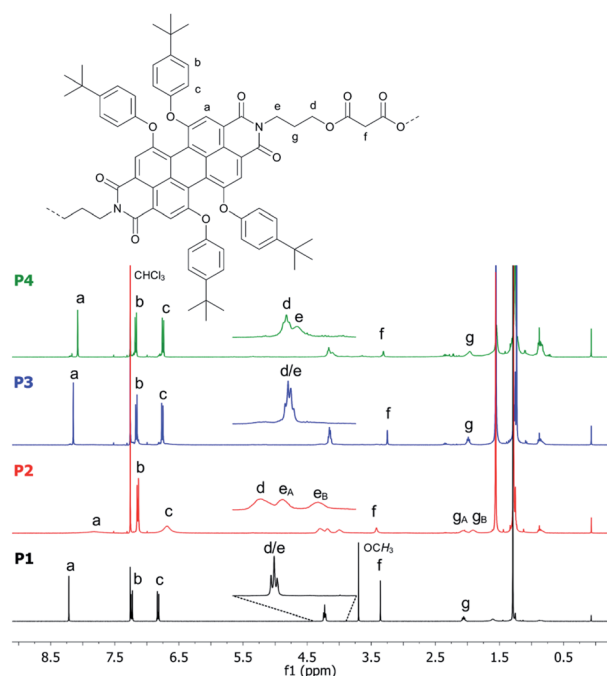
groups linked to oxygen and nitrogen (Fig. 2, d and e), and a pseudo quintet at 2.0 ppm for the central CH$_2$-group. A singlet was found for the malonate CH$_2$-groups at 3.3 ppm. The spectrum is completed with two singlets for OCH$_3$ and *tert*-butyl groups at 3.7 and 1.3 ppm, respectively. For **P3** and **P4**, the same set of signals was observed reflecting the high symmetry of D_{2h} for **P1**, D_{3h} for **P3**, and D_{4h} for **P4**. In contrast, the ^{1}H-NMR spectrum of **P2** is rather different. All signals are strongly broadened or barely visible (Fig. 2, second row). Additionally, a split of the signals for the OCH$_2$- and the central CH$_2$-groups (Fig. 2, e$_A$, e$_B$ g$_A$, g$_B$) is observed. Obviously, atropisomerization is slow at the NMR timescale.

To further investigate the dynamic behaviour and to understand the stereo-chemical consequences, we conducted

Fig. 3 Temperature-dependent ^{1}H NMR (600 MHz) spectra of **P2** recorded in C$_2$D$_2$Cl$_4$.

Fig. 2 Comparison of the ^{1}H NMR (400 MHz) spectra of **P1** (bottom), **P2**, **P3** and **P4** (top) recorded in CDCl$_3$ at room temperature.
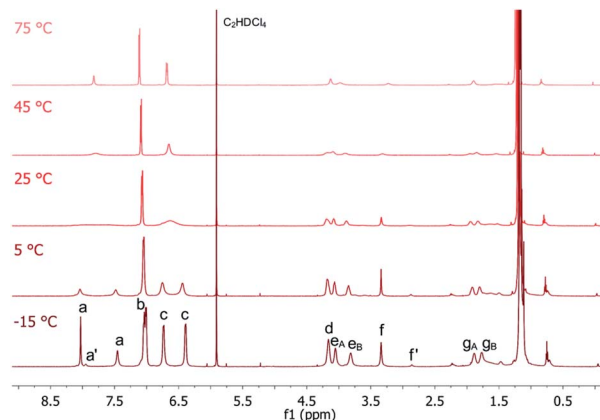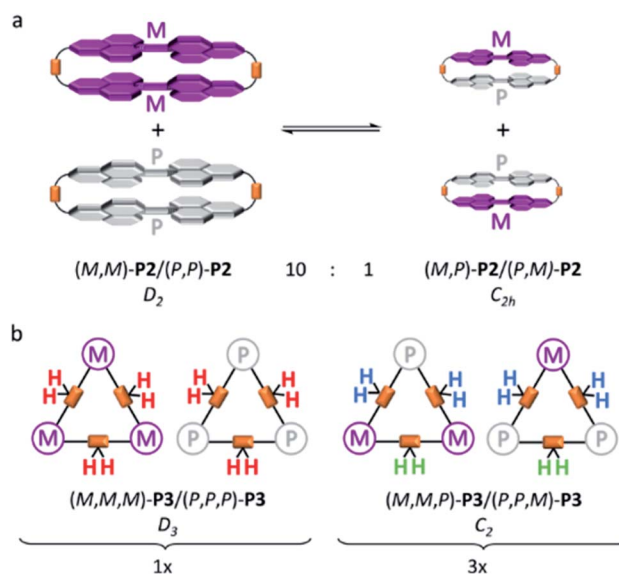

Fig. 4 Schematic representation of conformational equilibrium between the homochiral (M,M)-**P2**/(P,P)-**P2** and the achiral mesocate (M,P)-**P2**/(P,M)-**P2** with a ratio of 10 : 1 in C$_2$D$_2$Cl$_4$ at −15 °C (a) and statistical distribution of (M,M,M)-**P3**/(P,P,P)-**P3** and (M,M,P)-**P3**/(P,P,M)-**P3** of 1 : 3 (b).

a detailed NMR study of **P2** and **P3** at high and low temperatures. Upon cooling of **P2** in [D2]-tetrachloroethane we observed a sharpening of the peaks and a splitting of the signals in the aromatic region, most clearly visible at −15 °C (Fig. 3). Here, the epimerization *via* a butterfly twist of the perylene is slow on the NMR timescale. In principle, **P2** exists as a racemic mixture of two diastereoisomers, homochiral (M,M)-**P2**/(P,P)-**P2** and mesocate (M,P)-**P2**/(P,M)-**P2** (Fig. 4a). In the ^{1}H NMR spectrum, we attribute the main signals to the racemic mixture of homochiral (M,M)-**P2**/(P,P)-**P2** for the following reason. Here, the symmetry is reduced to D_2 and, consequently, the protons of the PBIs (Fig. 3, a) as well as the protons of the aromatic bay-substituents (Fig. 3, b and c) form two heterotopic sets of four and eight homotopic protons, respectively.

We distinguish between one set of protons, which protrudes into the cage of the cyclophane (*endo*) and one set which protrudes from it (*exo*). The protons of the alkyl chains in this environment are diastereotopic and due to the presence of three C_2-axes again two sets of four homotopic protons for each CH$_2$-group appear (Fig. 3, e$_{A/B}$ and g$_{A/B}$). For one methylene-group (Fig. 3, f), no splitting was observed due to isochrony. Interestingly, the malonate protons are homotopic, because they are interchanged by the three C_2-axes. Consequently, they appear as one singlet. This would also happen, if diastereotopic protons are isochronous. However, upon close inspection of the ^{1}H-NMR at −15 °C we found additional signals for the PBI- (Fig. 3, a') and malonate-protons (Fig. 3, f'), which we attribute to the achiral mesocate (M,P)-**P2**/(P,M)-**P2**.

Due to the presence of a mirror plane (point group C_{2h}) this diastereomer is achiral. But, no symmetry element interchanges the malonate-protons. These appear as two doublets ($^2J_{HH} = 17$ Hz), best visible at −5 °C, and make our assignment unambiguous (Fig. S5 in the ESI‡). To prove that this signal group belongs to the different diastereoisomers of **P2**, we performed 1D-EXSY in the rotating frame at 5 °C (Fig. S6 in the ESI‡). Upon irradiation of each signal group exchange peaks appeared, showing the slow interconversion of (M,P)-**P2** and its enantiomer into (M,M)-**P2** and its enantiomer and *vice versa*.

The integral ratio between (M,M)-**P2**/(P,P)-**P2** and (M,P)-**P2**/(P,M)-**P2** is 10 : 1 in C$_2$D$_2$Cl$_4$ at −15 °C (Fig. S7 in the ESI‡). Such an impressive diastereoselectivity for (M,M)-**P2**/(P,P)-**P2** is rationalized on grounds of attractive π–π interactions between the PBIs which are facilitated by the flexible linkers. This is even more pronounced in the case of **P2F2$_{Et}$**. No evidence for the presence of (M,P)-**P2F2$_{Et}$**/(P,M)-**P2F2$_{Et}$** in a variable temperature ^{1}H NMR assays was gathered (Fig. S8 in the ESI‡). Furthermore, the diastereoselectivity is solvent dependent. In CD$_2$Cl$_2$ only (M,M)-**P2**/(P,P)-**P2** is present as shown in Fig. S9 (in the ESI‡). The homochiral self-assembly has been previously observed in solid crystal structures[47] and under chiral guest encapsulation conditions.[17] However, to the best of our knowledge, this is the first time that it is observed quantitatively in solution without the need for any particular guest requirements.

Upon heating, every set of signals coalesces for **P2** and **P2F2$_{Et}$** to yield spectra, which are comparable to those of high symmetric molecules of point group D_{2h}. Coalescence temperatures were higher for **P2F2$_{Et}$** indicating a higher inversion

barrier (Fig. S8 in the ESI‡). To quantify this observation, the activation energy $\Delta G^{\ddagger}$ for the conformational interconversion of the diastereomers was calculated for **P2** and **P2F2$_{Et}$** in CD$_2$Cl$_2$ and C$_2$D$_2$Cl$_4$ using the coalescence method. The associated equation and the respective coalescence temperatures as well as chemical shifts are listed in the ESI (Table S1‡). In both solvents, the activation energy for **P2** ($\Delta G^{\ddagger}$ (CD$_2$Cl$_2$) = 52.8 kJ mol^{-1} and $\Delta G^{\ddagger}$ (C$_2$D$_2$Cl$_4$) = 57.0 kJ mol^{-1}) is lower than that of **P2F2$_{Et}$** ($\Delta G^{\ddagger}$ (CD$_2$Cl$_2$) = 61.3 kJ mol^{-1} and $\Delta G^{\ddagger}$ (C$_2$D$_2$Cl$_4$) = 64.0 kJ mol^{-1}). **P2** is less sterically hindered than **P2F2$_{Et}$** and has a high flexibility due to the malonate linker, which favours the interconversion process. Even the values for the sterically much more demanding **P2F2$_{Et}$** are lower than the free energy for a comparable PBI cyclophane with rigid linkers ($\Delta G^{\ddagger}$ (C$_2$D$_2$Cl$_4$) = 68.7 kJ mol^{-1}).[17]

In contrast to **P2** and **P2F2$_{Et}$**, **P3** shows no sharpening at higher temperatures (Fig. S10 in the ESI‡). However, we note an interesting behaviour for **P3** at low temperatures. Upon cooling, signals in the ^{1}H-NMR as well as in the ^{13}C-NMR spectra broaden and finally split. To understand the aforementioned thorough symmetry analyses of all isomers together with statistics are necessary. Like **P2**, **P3** exists as a racemic mixture of two diastereoisomers, that is, homochiral (M,M,M)-**P3**/(P,P,P)-**P3** and (M,M,P)-**P3**/(P,P,M)-**P3** (Fig. 4b). Homochiral **P3** shows D_3 symmetry. In contrast to **P2**, the PBIs of **P3** are free to rotate around the flexible linkers. In other words, a single set is expected for the PBI protons.

The protons of the three CH$_2$ alkyl groups are diastereotopic, but the malonate protons are not (Fig. 4b, red protons). As they are in line with the C_2-axes they are all interchanged by action of the C_3- and the three C_2-axes. Consequently, one singlet for this set of homotopic protons is expected. (M,M,P)-**P3**/(P,P,M)-**P3** has only one C_2-axis and is of point group C_2. Therefore, two singlets in a 2 : 1 ratio for the PBI protons are expected. The malonate protons are a special case. In two out of the three CH$_2$-groups the protons are diastereotopic (Fig. 4b, blue protons). But, the third is again in line with the C_2-axis (Fig. 4b, green protons) and, therefore, homotopic. Thus, we expected two doublets
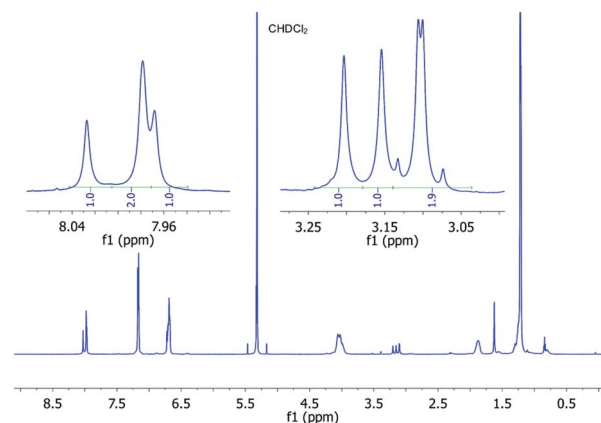

Fig. 5 ^{1}H (600 MHz) NMR spectrum of **P3** dissolved in CD$_2$Cl$_2$ recorded at −20 °C showing the typical ratio of 1 : 1:2 for the perylene and malonate protons.

from the AB-spin system (Fig. 4b, blue protons) and one singlet (Fig. 4b, green protons) in a 2 : 1 ratio. Fig. 5 shows the ^{1}H-NMR spectrum of **P3** at −20 °C with the described splitting for all protons. For the ^{13}C-NMR spectra see Fig. S11 (in the ESI‡).

The splitting and the multiplicity of the signals are both in perfect agreement with our symmetry considerations. The unexpected integral ratio of 1 : 1 : 2 needs, however, explanation. Considering only symmetry, a mixture without any preference for one diastereoisomer would yield a proton spectrum with an integral ratio of 3 : 2 : 1 for each signal group. But, when taking statistics into account (M,M,P)-**P3**/(P,P,M)-**P3** would be three times more populated than (M,M,M)-**P3**/(P,P,P)-**P3**. Thus, an integral ratio of 1 : 1 : 2 would result for each signal group, which is in sound agreement with the experiments. For **P3**, in contrast to **P2**, no preference for one of the diastereoisomers is observed. This can be rationalized from the fact that in the three-PBI cyclophane a conformation with two PBIs in close contact with each other is less favored. In the C_2-symmetrical **P3**, two branches of the alkyl chain and two of the PBIs cannot be interchanged. For the third branch, this is possible by action of the C_2-axis, which is why an additional splitting with a total ratio of 1 : 1 : 1 : 1 is expected. Interestingly, this does not apply to the malonate CH$_2$-groups. They are located in the middle between the two branches and the ratio, thus, remains at 2 : 1 : 1. This additional splitting in the third branch was detected for one of the PBI carbon atoms and for the OCH$_2$-group at even lower temperatures of −38 °C (Fig. S12 in the ESI‡). To prove that all signal groups belong to the different diastereoisomers of **P3**, we performed 1D-EXSY for the malonate resonances in the rotating frame at −20 °C. Exchange peaks appeared when each signal group was irradiated. This is exemplified for the selective excitation at 3.24 ppm in Fig. S13 (in the ESI‡). It displays the slow interconversion of (M,M,M)-**P3** and its enantiomer into (M,M,P)-**P3** and its enantiomer and *vice versa*.

Steady-state absorption and fluorescence spectroscopy

Steady-state absorption and fluorescence spectra of **P1**, **P2**, **P3**, and **P4** measured in toluene are shown in Fig. 6. **P1** reveals the characteristic S$_0$–S$_1$ PBI features in the 500 to 600 nm range,

that is, a set of absorption maxima at 534 and 575 nm, corresponding to the 0–*1 and 0–*0 vibrational transitions. In the 450 nm region, the weaker absorptions are attributed to the S$_0$–S$_2$ transitions. In **P2**, the 0–*1 vibrational transition is more pronounced than in **P1**, with a 0.99-to-1 ratio of the corresponding 0–*1 and 0–*0 intensities, respectively. At this point we infer H-type excitonic coupling due to the co-facial stacking of the two PBIs.[15,48] According to exciton theory, transitions to the lower-energy exciton-split LUMO, which corresponds to the 0–*0 transition, are symmetrically forbidden in face-to-face stacked PBIs. Instead, transitions to the higher-energy exciton-split LUMOs, which relate to the 0–*1 transition, take the complete oscillator strength.[16]

PBI stacking in **P2** deviates, however, from the ideal scenario. It is the presence of the bulky phenoxy substituents at the bay positions that evokes non-planar PBIs. Considering that the 0–*0 transitions are discernible in **P2** a subtle interplay between excitonic and vibronic couplings relieves the symmetry restrictions.[49] Intermolecular aggregation of **P2** was ruled out by means of corroborating that the absorption features were found to be concentration independent (Fig. S39 in ESI‡). This is in agreement with the fact that the sterically demanding tetra-(4-*tert*-butylphenoxy) substituents cause significant structural distortions and, in turn, suppress the tendency towards aggregation.[48]

When turning to **P3** and **P4**, both 0–*1 and 0–*0 transitions are seen with, however, different relative intensities. The intensity ratio follows **P2** > **P4** > **P3**. This trend suggests that the flexible linkers of **P3** and **P4** permit loose co-facial PBI stackings. Solvent viscosity-dependent bathochromic shifts of the absorptions were observed when measured in tetrahydrofuran (THF), benzonitrile (PhCN), and 1,1,2,2-tetrachloroethane (TCE) next to toluene (Fig. S38 in the ESI‡).

Fig. 7 surveys the absorption and fluorescence spectra of **P1F2$_{Et}$** and **P2F2$_{Et}$** in toluene, and **P2F2$_{TEG}$** in toluene as well as 5% THF/water mixture. All **P1**-related absorption features were retained in **P1F2$_{Et}$**. No significant perturbations nor any additional transitions were seen. What was, however, observed was the absorbance increase at wavelengths below 400 nm. This
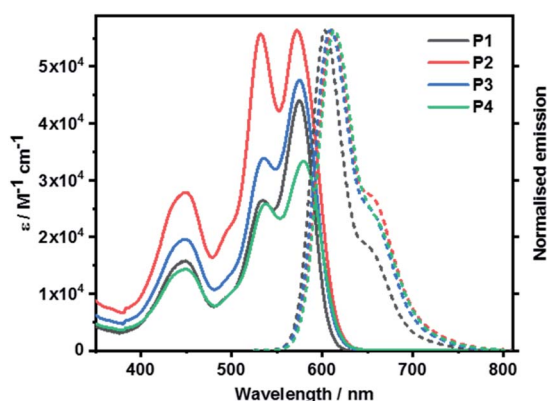

Fig. 6 Absorption and normalized fluorescence spectra of **P1** as well as cyclophanes **P2**, **P3**, and **P4** recorded in toluene at room temperature.
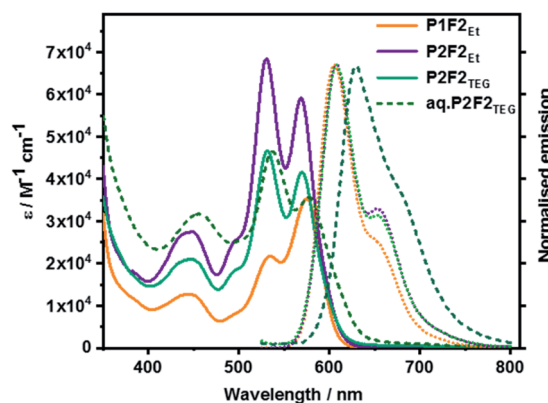

Fig. 7 Absorption and normalized fluorescence spectra of **P1F2$_{Et}$**, **P2F2$_{Et}$**, and **P2F2$_{TEG}$** recorded in toluene as well as **P2F2$_{TEG}$** recorded in 5% THF/water mixture (dashed line) at room temperature.

arises from the presence of the fullerenes. Co-facial π–π stacking is present in **P2F2$_{Et}$** and **P2F2$_{TEG}$**, as evidenced by 1.16-to-1 and 1.12-to-1 ratios of the corresponding 0–*1 and 0–*0 intensities, respectively. **P2F2$_{TEG}$** dissolved in a 5% THF/water mixture showed absorptions that are bathochromically shifted by ~7 nm compared to toluene solutions, which is a trend that has been reported for PBIs in an aqueous environment.[50,51] Here, hydrophobic interactions favor interchromophore stacking and result in an even higher intensity ratio of 1.31-to-1. The higher ratios seen in **P2F2$_{Et}$** and **P2F2$_{TEG}$** corroborate the stronger co-facial π–π stackings as seen, for example, in the NMR investigations. All maxima, molar extinction coefficients, and relative intensities of the 0–*1 and 0–*0 transitions in different solvents are listed in Table S2 (in the ESI‡).

Overall, all fluorescence maxima are Stokes-shifted by 30–35 nm. For example, **P1** shows a vibrationally resolved fluorescence spectrum with a maximum at 603 nm and a shoulder at 655 nm. **P2**, **P3**, and **P4** exhibit similar fluorescence features with slightly red-shifted maxima, that is, from 610 to 615 nm. No evidence for any excimer formation was, however, noted. The fluorescence quantum yields decrease from as high as 90% for **P1** to less than 26% for the cyclophanes (Table S3 in the ESI‡). Such a trend substantiates a π–π stacking-induced quenching of the PBI fluorescence. A remarkable de-intensification of the quantum yields is also observed when the solvent is changed from non-polar toluene to highly polar benzonitrile. Implicit is the involvement of symmetry-breaking charge transfer and/or symmetry-breaking charge separation, which opens up non-radiative deactivation pathways.[52] The emission spectral features of the model compound **P1F2$_{Et}$** and

cyclophane-fullerene hybrids **P2F2$_{Et}$** and **P2F2$_{TEG}$** in organic solvents exhibited no significant shifts compared to their pure PBI counterparts.

However, the fluorescence quantum yield is reduced to 40–50% in **P1F2$_{Et}$** in different organic solvents, suggesting excited state interactions of PBI with the attached fullerene pentakis-adducts. **P2F2$_{Et}$** and **P2F2$_{TEG}$** also exhibit solvent-dependent quenching much like what is seen for **P2**. Aqueous solutions of **P2F2$_{TEG}$** showed a broad and red-shifted fluorescence with a maximum at 630 nm, a shoulder at 685 nm, and a quantum yield of <1%.

Temperature-dependent absorption and fluorescence spectroscopic studies were performed with **P2** and **P3** in 1,1,2,2-tetrachloroethane and are gathered in Fig. S43 in the ESI.‡ Both **P2** and **P3** exhibit hypochromic as well as hypsochromic shifts in the absorption spectra upon heating. We rationalize this by the enhanced flipping of the naphthalenes of the PBI core at higher temperatures.[53] However, unlike **P3**, the ratio of 0–*1 to 0–*0 intensities of **P2** shows a subtle decrease towards higher temperature. This indicates weakening of the PBI π–π stackings. **P2** reveals a two-fold increase upon heating, whereas no significant changes are seen for **P3**. In other words, **P3** is less rigid than **P2** at any given temperature. This finding is in sound agreement with the low-temperature NMR results.

Transient absorption spectroscopy

To understand the solvent-sensitive excited state dynamics, femtosecond (fs) and nanosecond (ns) transient absorption (TA) studies were performed in toluene, THF and PhCN, by photo-exciting at 550 nm, with an OD of around 0.4 (Fig. S45–S51 in the ESI‡). In-depth analysis of the TA spectra was performed
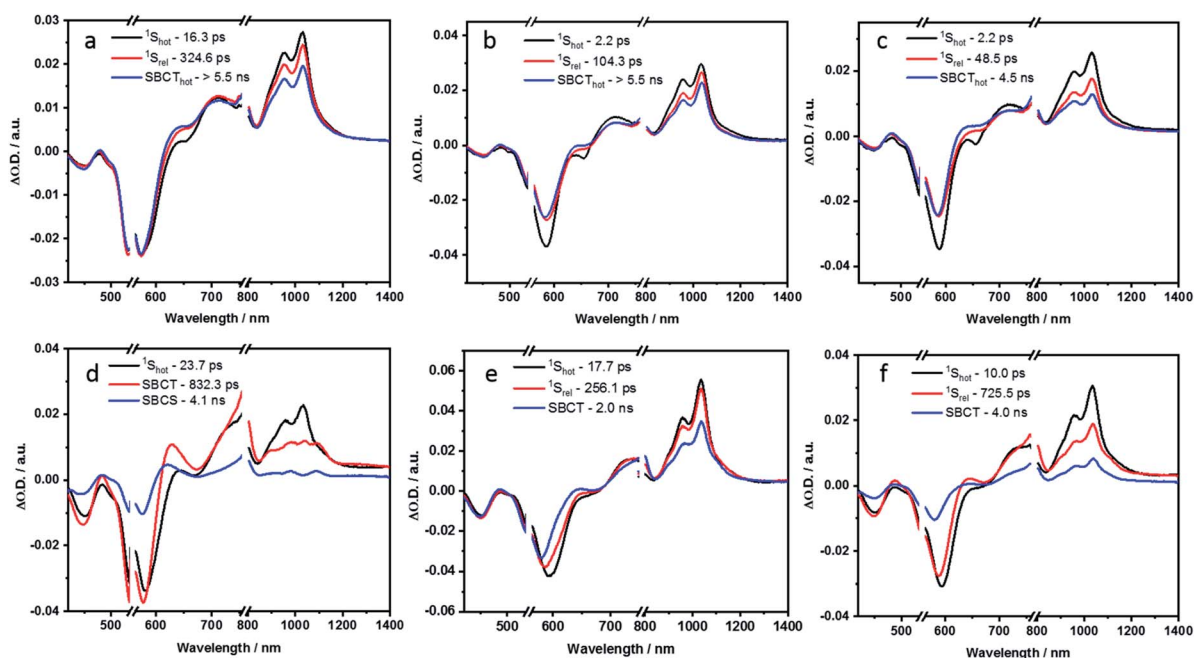

Fig. 8 Evolution associated spectra reconstructed from the sequential global analysis of fs-TA spectra of **P2**, **P3** and **P4** in toluene (a, b and c respectively) and PhCN (d, e and f respectively).

using the GloTarAn program.[54] Kinetic models with four or five species were employed to run the global sequential analysis. The resulting evolution associated spectra (EAS) and the relative population of the excited states are shown in the ESI.‡ To elucidate the deactivation pathway of **P1**, a kinetic model based on four species was employed (Fig. S52 and S53 in the ESI‡). To this end, **P1** shows in toluene the characteristic spectral signatures with ground state bleaching at 452 and 595 nm, singlet excited state absorptions at 700, 955, and 1038 nm, and stimulated emission at 652 nm. The first species, which is a vibrationally hot singlet excited state, transforms to a vibrationally relaxed excited state in 8.5 ps as the second species. It undergoes further relaxation to a third species in 350.6 ps. This third species is the fluorescent singlet excited state, which decays to the ground state with a lifetime of 6.0 ns. In line with a fluorescence quantum yield of 90% in toluene, **P1** decays primarily by fluorescence. Still, the remaining 10% is subject to intersystem crossing to afford the triplet excited state. From the ns-TA spectra, we conclude a lifetime of more than 350 μs. Regardless of the solvent polarity, similar kinetics were obtained for **P1**.

In contrast, **P2** exhibits distinct, solvent polarity-dependent spectral evolutions (Fig. S46 in the ESI‡). The EAS reconstructed from the global fits of fs-TA studies for **P2** in toluene and benzonitrile are shown in Fig. 8a and d.

In the non-polar toluene, the initial vibrationally hot singlet excited state, undergoes vibrational relaxation to form the second species in 16.3 ps and then proceeds to a new long-lived intermediate third species in 324.6 ps. By means of comparing the spectral features with the spectroelectrochemical absorptions of the PBI radical cation (630, 790, 975, and 1083 nm) and radical anion (685, 790, 975, and 1083 nm) (Fig. S44 in the ESI‡), the third species corresponds to the PBI$^{\delta+}$–PBI$^{\delta-}$ symmetry-

breaking charge transfer (SBCT) state. Its decay dynamics were probed using ns-TA measurements and the corresponding EAS spectra are shown in Fig. 9. Considering that the fourth species also features the SBCT fingerprints, we assign the third and fourth species to a hot SBCT and a relaxed SBCT, respectively. The PBI triplet excited state is the fifth species and is generated with a time constant of 14.7 ns. A weak positive absorption in the 500 nm region is the characteristic of the triplet excited state and it lives for 137 μs.

In polar PhCN, a different excited state relaxation pathway was concluded. Formation of the vibrationally hot excited state is followed by deactivation over a time of 23.7 ps to afford the SBCT state as first and second species, respectively. It lives for 832.3 ps and is characterized by broadening of the excited state absorption in the nIR region and an evolving maximum at 630 nm due to the formation of the PBI radical cation. The SBCT state then transitions to a symmetry-breaking charge-separated (SBCS) state with the respective markers at 630, 685, 790, 975, and 1085 nm. This is the third species. SBCS is unfavorable in non-polar toluene due to the positive free energy of charge separation.[55,56] Finally, it is with a time delay of 4.1 ns that the SBCS state populates the PBI triplet excited state as the fourth and final species. 118 μs is the lifetime, by which the triplet excited state decays back to the ground state. The decay kinetics observed for **P2** in THF, which has intermediate polarity, was very similar to that obtained in PhCN (Fig. S54 and S55 in the ESI‡).

In toluene, the excited state deactivation mechanism of **P3** and **P4** is similar to that gathered for **P2** in toluene. Excitation populates the first species, which is the singlet excited state but a high vibrational level of it, followed by the formation of a vibrationally relaxed state in 2.2 ps as the second species. It
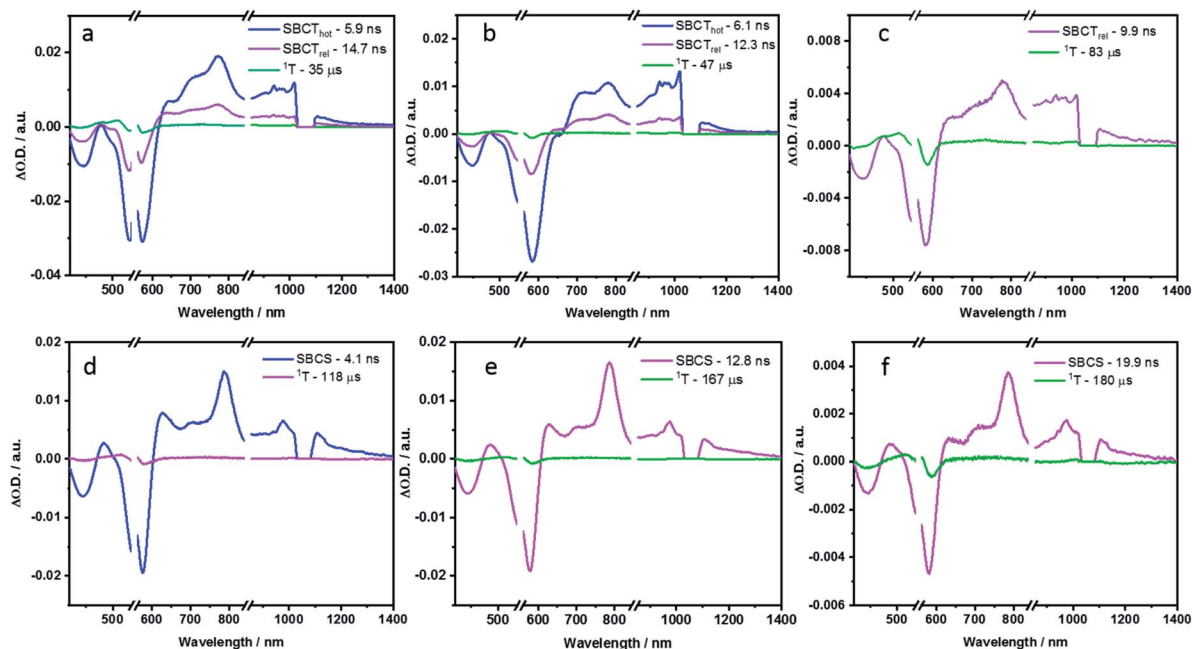

Fig. 9 Evolution associated spectra reconstructed from the sequential global analysis of ns-TA spectra of P2, P3 and P4 in toluene (a, b and c respectively) and PhCN (d, e and f respectively).

undergoes further relaxation within 104.3 ps for **P3** or 48.5 ps for **P4** to form the third species or the hot SBCT state with a dipolar character. The corresponding lifetimes are 6.1 and 4.5 ns in **P3** and **P4**, respectively. From the ns-TA spectra, it is evident that the hot SBCT state relaxes to the fourth species, which has a lifetime of 12.3 ns in **P3** and 9.9 ns in **P4**. Finally, this relaxed SBCT state decays to form the triplet excited state, which then repopulates the ground state in <100 μs.

In PhCN, photoexcitation populates the vibrationally hot singlet excited state of **P3**, which relaxes initially in 17.7 ps, and, which subsequently deactivates in 256.1 ps. This decay is concomitant with a remarkable blue-shift in the ground state bleaching. Within a time span of 2.0 ns, the SBCT state populates the SBCS state, featuring the fingerprint absorption bands of the PBI radical cation and radical anion. The SBCS state populates in 12.8 ns the triplet manifold, which exhibits a lifetime of 167 μs.

Unlike **P3**, the evolution associated spectrum of **P4** in PhCN resembles that of **P2** and requires the use of an additional species to fit the TA spectrum. In general, the difference is ascribed to the excited state geometry of **P4**. For **P4**, we hypothesize two pairs of π–π stacked PBIs. So, its behavior is expected to be similar to that of **P2**. For **P4** in PhCN, the vibrationally hot singlet excited state undergoes relaxation in 10 ps. By this, the second species, which has a slight dipolar character, is formed. It subsequently populates the SBCT, SBCS, and triplet excited states in 725.5 ps, 4.0 ns, and 19.9 ns, respectively. Finally, the triplet excited state decays back to the ground state with a lifetime of 180 μs. The deactivation mechanism in THF was comparable for **P3** and **P4** to those in PhCN, as shown in Fig. S56–S59 (in the ESI‡). Based on the results of TA spectral analyses, a simplified energy scheme for the excited state deactivation pathway of the cyclophanes in polar and non-polar solvents is summarized in Fig. 10. The estimated lifetime values are summarized in Tables S4 and S5 in the ESI.‡

For all cyclophanes, the population of the PBI triplet excited state from either SBCT in toluene or SBCS in benzonitrile was quantified by measuring the singlet oxygen phosphorescence at 1270 nm (Fig. S66 in ESI‡). Using C_{60} in air-equilibrated toluene as the reference,[57,58] the singlet oxygen quantum yields (Φ_Δ) were determined. They are summarized in Table S6.‡ In toluene, particularly high Φ_Δ values of 67% and 76% for **P2** and **P4** and a comparably low Φ_Δ value of 37% for **P3** correlate well with the fluorescence quantum yields. However, in benzonitrile, charge recombination from SBCS to afford the triplet excited state is reduced for **P2** and **P4** as indicated by Φ_Δ values of 53% and 44% for **P2** and **P4**, respectively. The differences relative to toluene are due to a competing charge-recombination pathway, by which the ground state is directly recovered. Only in **P3**, it is slightly increased to 43%.

Finally, we analyzed **P1F2$_{Et}$**, **P2F2$_{Et}$** and **P2F2$_{TEG}$** in polar and non-polar solvents. In particular, 550 nm excitation initiated the same excited state decay mechanism as observed for **P1** and **P2**, respectively. As such, we used the kinetic models, which proved to fit the data for **P1** and **P2** in different solvents quite well with four or five species. The fs-TA, ns-TA, and evolution associated spectra together with the relative population of the corresponding species are shown in Fig. S49–S51 and S60–S65 (in the ESI‡). Lifetimes of the species are summarised in Tables S4 and S5.‡ By virtue of 550 nm photoexcitation, which is selective for PBI, no fullerene-centered transients were detected. In contrast, when photoexciting the fullerenes at around 370 nm a resonance energy transfer by means of dipole–dipole interactions was concluded from the 3D fluorescence heat maps (Fig. S67 and S68 in the ESI‡).

Conclusions

PBI-based cyclophanes **P2**, **P3**, and **P4** with different sizes and various arrangements were synthesized and the relationship between the structure and properties was thoroughly investigated. By varying the reaction conditions and using TTF in an electron donor–acceptor templated synthesis, the yield of the two-PBI **P2** was improved from 2.7% to 8.1%, which is already a reasonably high yield in cyclophane synthesis. The changes in the NMR spectra indicate a different chemical environment in terms of π–π stacking PBIs in the cyclophanes. Remarkably, **P2** exhibits the diastereoselective formation of homochiral atropisomers (M,M)-**P2**/(P,P)-**P2** at low temperatures by virtue of the flexible linkers. Owing to the strong intramolecular π–π interactions between co-facially arranged PBIs, **P2** shows H-type excitonic coupling. Looser is the co-facial stacking of the PBIs within three-PBI and four-PBI cyclophanes. Therefore, at low temperatures, both diastereomeric pairs (M/M/M)-**P3**/(P,P,P)-**P3** as well as (M/M/P)-**P3**/(P,P,M)-**P3** are detected in the ^{1}H-NMR spectra of **P3**. Such a dynamic stacking is expected to provide an accessible cavity for hosting various molecular guests.

From a fluorescence quantum yield decrease in the order **P1** >> **P3** > **P4** > **P2** π–π stacking-induced quenching between the PBIs in their excited states was concluded. Moreover, the quantum yields are solvent-dependent. This suggests symmetry-breaking charge-transfer/charge-separation interactions.
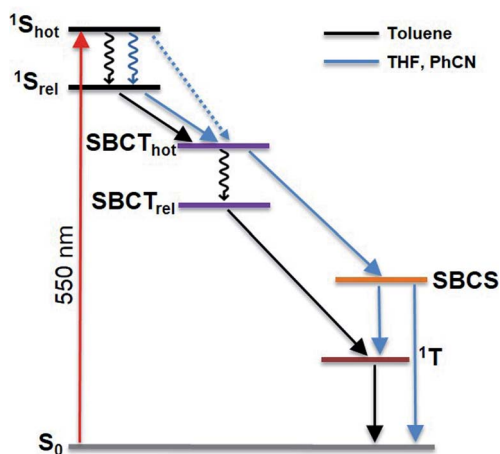

Fig. 10 Simplified energy diagram illustrating the excited state deactivation mechanism of the cyclophanes in polar and non-polar solvents. The black arrows represent the decay pathway in toluene. The blue arrows indicate the deviation observed in polar solvents THF and PhCN, which favour the formation of a stabilized SB-CS state.

Indeed, time-resolved pump-probe experiments helped to confirm the presence of both charge-transfer and charge-separation. With a temperature increase, **P2** is subject to a weakening of the π–π stacking PBIs. Of great value are the flexible malonate linkers in **P2** as they enabled the functionalization with hydrophobic as well as hydrophilic fullerene pentakisadducts. In this context, we synthesized for the first time a covalently linked PBI-cyclophane-fullerene hybrid. The solvent dependent coalescence temperatures as well as the activation energies for the conformational interconversion are higher for **P2F2$_{Et}$** than for **P2**, which is due to a sterically demanding fullerene. The enhanced co-facial π–π stacking present in the cyclophane-fullerene adducts **P2F2$_{Et}$** and **P2F2$_{TEG}$** leads to a complete diastereoselectivity for the case of **P2F2$_{Et}$**. This illustrates that the hybridization strategy with fullerenes allows us to modulate the cyclophanes with respect to solubility, stacking, cavity size, photophysics and sterical arrangement. Given the current undivided attention in dye-based cages for selective purification, sensing, catalysis or chiral recognition, our findings are of utmost interest.

Data availability

All experimental data associated to the article is given in the ESI.† Data have not been deposit in any repository.

Author contributions

I. Solymosi: investigation (synthesis and characterization); writing-original draft. S. Krishna: investigation (photophysics), writing-original draft. E. Nuin: conceptualization, investigation (synthesis), writing – review & editing. H. Maid: investigation (NMR characterization), writing – original draft. B. Scholz: investigation (precursor synthesis). D. M. Guldi: conceptualization, supervision, writing – review & editing, funding acquisition. M. E. Pérez-Ojeda: conceptualization, investigation (synthesis), supervision, writing – review & editing, funding acquisition. A. Hirsch: supervision, writing – review & editing, funding acquisition.

Conflicts of interest

There are no conflicts to declare.

Acknowledgements

Notes and references

¶ This dumbbell molecule was functionalized with unsubstituted [60]fullerene and cannot be used as a photophysical model for our systems given the different optical properties.

1 C. J. Brown and A. C. Farthing, *Nature*, 1949, **164**, 915–916.
2 D. J. Cram and H. Steinberg, *J. Am. Chem. Soc.*, 1951, **73**, 5691–5704.
3 F. Würthner, *Chem. Commun.*, 2004, **14**, 1564–1579.
4 D. H. Harris, S. Brixi, B. S. Gelfand, B. H. Lessard and G. C. Welch, *J. Mater. Chem. C*, 2020, **8**, 9811–9815.
5 J. D. Yuen, V. A. Pozdin, A. T. Young, B. L. Turner, I. D. Giles, J. Naciri, S. A. Trammell, P. T. Charles, D. A. Stenger and M. A. Daniele, *Dyes Pigm.*, 2020, **174**, 108014.
6 R. K. Gupta, A. Dey, A. Singh, P. K. Iyer and A. A. Sudhakar, *ACS Appl. Electron. Mater.*, 2019, **1**, 1378–1386.
7 W. Yan, Z. He, J. Jiang, D. Lu, Y. Gong, W. Yang, R. Xia, W. Huang and H. Xin, *J. Mater. Chem. C*, 2020, **8**, 14773–14781.
8 R. Xin, C. Zeng, D. Meng, Z. Ren, W. Jiang, Z. Wang and S. Yan, *ACS Omega*, 2020, **5**, 18449–18457.
9 J. Huang, H. Ren, R. Zhang, L. Wu, Y. Zhai, Q. Meng, J. Wang, Z. Su, R. Zhang, S. Dai, S. Z. D. Cheng and M. Huang, *ACS Nano*, 2020, **14**, 8266–8275.
10 M. Hecht, P. Leowanawat, T. Gerlach, V. Stepanenko, M. Stolte, M. Lehmann and F. Würthner, *Angew. Chem., Int. Ed.*, 2020, **59**, 17084–17090.
11 P. Spenst and F. Würthner, *J. Photochem. Photobiol., C*, 2017, **31**, 114–138.
12 P. Spenst and F. Würthner, *Angew. Chem., Int. Ed.*, 2015, **54**, 10165–10168.
13 H. Langhals and R. Ismael, *Eur. J. Org. Chem.*, 1998, **9**, 1915–1917.
14 W. Wang, L. Wang, B. J. Palmer, G. J. Exarhos and A. D. Q. Li, *J. Am. Chem. Soc.*, 2006, **128**, 11150–11159.
15 F. Schlosser, M. Moos, C. Lambert and F. Würthner, *Adv. Mater.*, 2013, **25**, 410–414.
16 J. Feng, Y. Zhang, C. Zhao, R. Li, W. Xu, X. Li and J. Jiang, *Chem.–Eur. J.*, 2008, **14**, 7000–7010.
17 M. Sapotta, P. Spenst, C. R. Saha-Möller and F. Würthner, *Org. Chem. Front.*, 2019, **6**, 892–899.
18 M. Weh, J. Rühe, B. Herbert, A.-M. Krause and F. Würthner, *Angew. Chem., Int. Ed.*, 2021, **60**, 15323–15327.
19 T. A. Barendt, W. K. Myers, S. P. Cornes, M. A. Lebedeva, K. Porfyrakis, I. Marques, V. Félix and P. D. Beer, *J. Am. Chem. Soc.*, 2020, **142**, 349–364.
20 W. Wang, A. D. Shaller and A. D. Q. Li, *J. Am. Chem. Soc.*, 2008, **130**, 8271–8279.
21 P. Spenst, A. Sieblist and F. Würthner, *Chem.–Eur. J.*, 2017, **23**, 1667–1675.
22 J. Rühe, D. Bialas, P. Spenst, A.-M. Krause and F. Würthner, *Org. Mater.*, 2020, **2**, 149–158.
23 F. Schlosser, J. Sung, P. Kim, D. Kim and F. Würthner, *Chem. Sci.*, 2012, **3**, 2778–2785.
24 P. Spenst, R. M. Young, B. T. Phelan, M. Keller, J. Dostál, T. Brixner, M. R. Wasielewski and F. Würthner, *J. Am. Chem. Soc.*, 2017, **139**, 2014–2021.
25 M. E. Pérez-Ojeda, I. Wabra, C. Böttcher and A. Hirsch, *Chem.–Eur. J.*, 2018, **24**, 14088–14100.
26 Y. Sun and Z. Li, *Polym. Chem.*, 2017, **8**, 4422–4427.
27 E. Nuin, V. Lloret, K. Amsharov, F. Hauke, G. Abellán and A. Hirsch, *Chem.–Eur. J.*, 2018, **24**, 4671–4679.

28 J.-J. Shim, C.-W. Lee and M.-S. Gong, *Synth. Met.*, 2001, **124**, 435–441.

29 C.-W. Lee, S.-W. Joo, J. Ko, J.-S. Kim, S.-S. Lee and M.-S. Gong, *Synth. Met.*, 2002, **126**, 97–104.

30 N. Chronakis, T. Brandmüller, C. Kovacs, U. Reuther, W. Donaubauer, F. Hampel, F. Fischer, F. Diederich and A. Hirsch, *Eur. J. Org. Chem.*, 2006, **10**, 2296–2308.

31 K. Ziegler, H. Eberle and H. Ohlinger, *Liebigs Ann. Chem.*, 1933, **504**, 94–130.

32 R. Hoss and F. Vögtle, *Angew. Chem., Int. Ed. Engl.*, 1994, **33**, 375–384.

33 J. C. Barnes, M. Juríček, N. A. Vermeulen, E. J. Dale and J. F. Stoddart, *J. Org. Chem.*, 2013, **78**, 11962–11969.

34 D. Canevet, M. Sallé, G. Zhang, D. Zhang and D. Zhu, *Chem. Commun.*, 2009, **17**, 2245–2269.

35 H. Y. Au-Yeung, P. Pengo, G. D. Pantoș, S. Otto and J. K. M. Sanders, *Chem. Commun.*, 2009, **4**, 419–421.

36 M. R. Bryce, G. J. Marshallsay and A. J. Moore, *J. Org. Chem.*, 1992, **57**, 4859–4862.

37 F. Würthner and A. Sautter, *Chem. Commun.*, 2000, **6**, 445–446.

38 F. Diederich and P. J. Stang, *Templated Organic Synthesis*, John Wiley & Sons, 2000.

39 Y. Nakamura, S. Minami, K. Iizuka and J. Nishimura, *Angew. Chem., Int. Ed.*, 2003, **42**, 3158–3162.

40 X. Camps and A. Hirsch, *J. Chem. Soc., Perkin Trans. 1*, 1997, **11**, 1595–1596.

41 K. L. Maxouti and A. Hirsch, *Eur. J. Org. Chem.*, 2018, **2018**, 2579–2586.

42 F. Beuerle and A. Hirsch, *Chem.–Eur. J.*, 2009, **15**, 7434–7446.

43 P. Witte, F. Hörmann and A. Hirsch, *Chem.–Eur. J.*, 2009, **15**, 7423–7433.

44 D. M. Guldi, B. M. Illescas, C. M. Atienza, M. Wielopolski and N. Martín, *Chem. Soc. Rev.*, 2009, **38**, 1587–1597.

45 F. Würthner, *Pure Appl. Chem.*, 2006, **78**, 2341–2349.

46 J. Schönamsgruber and A. Hirsch, *Eur. J. Org. Chem.*, 2015, **2015**, 2167–2174.

47 P. U. Osswald, PhD thesis, Julius-Maximilians-Universität Würzburg, Germany, 2007.

48 W. Kim, A. Nowak-Król, Y. Hong, F. Schlosser, F. Würthner and D. Kim, *J. Phys. Chem. Lett.*, 2019, **10**, 1919–1927.

49 R. L. Fulton and M. Gouterman, *J. Chem. Phys.*, 1964, **41**, 2280–2286.

50 F. Würthner, C. R. Saha-Möller, B. Fimmel, S. Ogi, P. Leowanawat and D. Schmidt, *Chem. Rev.*, 2016, **116**, 962–1052.

51 M. Sapotta, A. Hofmann, D. Bialas and F. Würthner, *Angew. Chem., Int. Ed.*, 2019, **58**, 3516–3520.

52 J. M. Giaimo, A. V. Gusev and M. R. Wasielewski, *J. Am. Chem. Soc.*, 2002, **124**, 8530–8531.

53 C. Kaufmann, D. Bialas, M. Stolte and F. Würthner, *J. Am. Chem. Soc.*, 2018, **140**, 9986–9995.

54 J. J. Snellenburg, S. P. Laptenok, R. Seger, K. M. Mullen and I. H. van Stokkum, *J. Stat. Softw.*, 2012, **49**, 1–22.

55 P. Spenst, R. M. Young, M. R. Wasielewski and F. Würthner, *Chem. Sci.*, 2016, **7**, 5428–5434.

56 J. Kong, W. Zhang, G. Li, D. Huo, Y. Guo, X. Niu, Y. Wan, B. Tang and A. Xia, *J. Phys. Chem. Lett.*, 2020, **11**, 10329–10339.

57 L. Biczok, H. Linschitz and R. I. Walter, *Chem. Phys. Lett.*, 1992, **195**, 339–346.

58 S. Foley, M. N. Berberan-Santos, A. Fedorov, D. J. McGarvey, C. Santos and B. Gigante, *J. Phys. Chem. A*, 1999, **103**, 8173–8178.